Thermal degradation and optical characteristics of plasticized poly(vinyl chloride-co-vinyl acetate-co-2-hydroxypropyl acrylate) terpolymer

Mahdy M. Elmahdy[1,2,*] (iD), Moustafa. T. Ahmed[1,3], Khalid A. Aldhafeeri[1], Maged A. Azzam[4], and Tarek Fahmy[3]

[1] Department of Physics, College of Science and Humanities in Al-Kharj, Prince Sattam bin Abdulaziz University, Al-Kharj 11942, Saudi Arabia
[2] Department of Physics, Faculty of Science, Mansoura University, Mansoura 35516, Egypt
[3] Polymer Research Group, Department of Physics, Faculty of Science, Mansoura University, Mansoura 35516, Egypt
[4] Department of Chemistry, College of Science and Humanities in Al-Kharj, Prince Sattam bin Abdulaziz University, Al-Kharj 11942, Saudi Arabia

ABSTRACT

Casting method was employed to prepare films of poly(vinyl chloride-co-vinyl acetate-co-2-hydroxypropyl acrylate) (PVVH) terpolymer doped with different amounts of tetrabutylammonium tetrafluoroborate ([TBA][BF$_4$]) electrolyte. The interaction between terpolymer and electrolyte was evident in the shift and reduction of the ATR-FTIR peak intensities of the C–Cl stretching vibrations at 613 cm^{-1} and 688 cm^{-1} with increasing electrolyte concentration. The effect of electrolyte was also visible in the reduction of DTG/DTA peak temperature (T_P) of the second stage of the composites. The decrease of the DSC glass transition temperature (T_g) from 344 K to 310 with increasing electrolyte content indicates the plasticization effect of the electrolyte that reduces the inter- and intramolecular interaction maintaining the flexibility of the PVVH terpolymer backbone to bend and slide more readily. The kinetics of thermal degradation of pure compounds and their composites were investigated and discussed in terms of the Coats–Redfern approach. The results revealed an increase in the activation energy of thermal degradation with increasing the electrolyte content. Linear and nonlinear optical parameters were calculated and discussed in terms of the single oscillator model and Miller's rule. The visible and UV transmittance of the investigated materials demonstrated values of 91% and 5%, respectively. Furthermore, they achieved reflectance of 3 and 58% in the visible and UV regions, respectively, making these composites an excellent candidate for optical applications. Besides, the optical conductivity (σ_{op}) and dielectric constant of all samples were investigated.

Address correspondence to E-mail: elmahdy@mans.edu.eg

🙋 Springer

1 Introduction

Nowadays, synthetic and natural polymer-based electrolytes have gained considerable interest and momentum in terms of studying their optical and electrical properties due to their use in many applications such as batteries, capacitors, and fuel cells [1–3]. The nature of the interaction of light with these new materials is of great interest, especially when switching from solar cells to light-emitting devices [4]. Those polymers that possess unique optical properties encourage researchers to consider them for use in optical devices and sensors [5].

Doping polymers with metals and electrolytes can enhance their physical properties paving the way for novel applications [2, 6]. For example, a PVVH/poly(ethyl methacrylate) blend filled with gold nanoparticles was used as a corrosion inhibitor for API 5L X70 carbon steel [7]. Another study exploited the high sensitivity of PVVH to the fluctuations of environment temperature to fabricate nanogenerators from zinc oxide (ZnO) nanowires that aligned vertically in the PVVH matrix [8]. Polymer electrolytes (PE) with low T_g achieve higher ionic conductivity and are favorable for commercial applications [9–12]. It was reported that the ionic conductivity increased by two orders of magnitude by using PE based on a low T_g poly(methyl siloxane) backbone [9]. The relationship between ionic conductivity and dielectric constant was also investigated by Imbrogno et al. [11] for poly(vinyl ether) lithium electrolytes and found an increase in ionic conductivity with increasing dielectric constant. The high electrical conductivity of PE was attributed to the lower lattice energy of electrolytes. The lower lattice energies of both polymer and electrolyte will increase the resulting polymer electrolyte stability. Hence, the dissolution of electrolytes in the polymer chains will be facilitated when the polymer has high dielectric and the salt has low lattice energy.

The thermal degradation of polymers is the change of the chemical structure at elevated temperatures without the concurrent inclusion of another compound [13]. The study of the thermal decomposition of polymeric materials is essential for developing rational polymer processing techniques, using polymers at high temperatures, and understanding thermal degradation mechanisms for the synthesis of refractory polymeric materials [14–16]. Thermal degradation of polymers can be divided into three types: (i) complete degradation accompanied by main chain breaking, (ii) side chain rupture with the formation of char residue and volatile products, and (iii) degradation with large amounts of char and little volatiles. For example, the thermal degradation of polyvinyl chloride (PVC) starts with the side group elimination leaving a polyene macromolecule that experiences reactions to form aromatic molecules [13].

The quaternary tetrabutylammonium tetrafluoroborate ([TBA][BF$_4$]) electrolyte is basically consisting of tetrabutylammonium (organic) cation and tetrafluoroborate (inorganic) anion and has the chemical form $[C_{16}H_{36}N]^+[BF_4]^-$. It is a water-soluble electrolyte with a high degree of inter-and intra-molecular hydrogen bonding. It has been successfully used extensively in electrochemistry, not only as a supporting electrolyte in aqueous and non-aqueous solvent systems but also in many different electrochemical methods of analytical and industrial interest [17–19]. Poly(vinyl chloride-co-vinyl acetate-co-2-hydroxypropyl acrylate) (PVVH) is an amorphous terpolymer with a sensitive chemical structure to temperature change. It is widely used in solid-state sensors, polyions, membranes, nanogenerators, and corrosion inhibitors [7, 8]. In the literature, some articles dealt with the investigation of the relaxation phenomenon of PVVH as pure material or with another polymer as a polymer blend [20–22], but there is a dearth of articles studying its optical properties [7, 8, 23–25].

In this contribution, we have prepared PVVH/[TBA][BF$_4$] terpolymer electrolytes with a different weight content of [TBA][BF$_4$] using the casting method. The selection of PVVH was based on its flexibility and sensitivity to the change in temperature, while [TBA][BF$_4$] electrolyte has numerous analytical and industrial applications. The purpose of this study is to trace the change in structure, thermal properties, and optical characteristics of PVVH due to adding the electrolyte in different concentrations. The change in structure was probed by ATR-FTIR while TGA/DTA, DSC, and UV–Vis. measurements were employed to investigate the thermal and optical characteristics. TGA/DTA and DSC revealed a reduction in peak (T_p) and glass transition (T_g) temperatures with increasing electrolyte concentration. On the other hand, UV–Vis measurements demonstrated high values of transmittance ($\sim$ 91%) in the visible spectrum and low values ($\sim$ 5%) in the UV

region. Furthermore, they achieved reflectance of 3 and 58% in the visible and UV regions, respectively. These results are promising and make these composites an excellent candidate for optical applications. Linear and nonlinear optical parameters were calculated and discussed in terms of the single oscillator model and Miller's rule.

2 Experimental

2.1 Materials and terpolymer electrolyte preparation

The poly(vinyl chloride-co-vinyl acetate-co-2-hydroxypropyl acrylate) (PVVH) with low molecular weight [$M_n \sim$ 33,000 g mol^{-1}; 81 wt% vinyl chloride (VC); 4 wt% vinyl acetate (VAc); 15 wt% 2-hydroxylpropyl acrylate (2HPA)] was purchased from Sigma-Aldrich while Tetrabutylammonium tetrafluoroborate ([TBA][BF$_4$]) with molecular weight of 329.27 g mol^{-1} was ordered from Merck. Tetrahydrofuran (THF) was used as a common solvent for PVVH and [TBA][BF$_4$] electrolytes. The latter was added to PVVH in different proportions (1 wt%, 2.5 wt%, 5 wt%, 10 wt%, 15 wt%, and 20 wt%) in THF with continuous stirring for about 3 h to get a homogeneous mixture. The mixture was poured into a glass petri dish and kept in a vacuum oven for about 24 h at 50 °C.

2.2 Characterization techniques

2.2.1 ATR-FTIR spectroscopy

Spectra of ATR-FTIR were recorded by Thermo Scientific iD5 ATR spectrometer in the wavenumber ranging from 500 to 4000 cm^{-1} and spectral resolution of 1 cm^{-1}. Measurements were executed in ambient air at room temperature. Pure PVVH and its composites were measured by placing a small piece of the sample on top of the diamond ATR crystal and collecting the spectra 100 times to achieve a better signal-to-noise ratio.

2.2.2 Thermogravimetric analysis (TGA/DTG)

Thermal degradation of PVVH, [TBA][BF$_4$] and their composites were monitored by Netzsch TG 209 F1 Libra Thermogravimetric analyzer (TGA) in the temperature range from 23 to 800 °C in steps of 10 °C min^{-1} under nitrogen atmosphere. An appropriate amount of the sample was placed in crucibles made of alumina (Al$_2$O$_3$) and the nitrogen gas flowed at a constant rate of 20 ml min^{-1}.

2.2.3 Differential scanning calorimetry (DSC)

Netzsch DSC 214 was employed to probe the thermal characteristics of PVVH with a heating/cooling rate of 10 °C min^{-1}. The samples were first heated from 298 to 473 K and then cooled down to 223 K at the same rate. The heat flow was recorded during the cooling run to overcome the thermal history of the samples and adsorbed water.

2.2.4 UV–Vis spectroscopy

Absorption of UV–Vis radiation by PVVH and its composites was traced by the ATi Unicam UV/Vis spectrophotometer in the wavelength range from 200 to 1100 nm and bandwidth of five nm. UV–Vis spectra were collected in ambient air at room temperature.

3 Results and discussion

3.1 ATR-FTIR spectroscopy

Figure 1a shows the ATR-FTIR transmission spectra for PVVH and its composites in the wavenumber range 4000–500 cm^{-1} at room temperature. Symmetric and asymmetric C-H stretching vibrations of methylene groups are detected at high wavenumbers from 2972 to 2980 cm^{-1} while the hydroxyl groups (OH) of 2-hydroxypropyl acrylate (2HPA) perform stretching vibrations at 3415 cm^{-1} [25–28]. The intensity of the higher wavenumber peaks (2877, 2908, 2938, and 2961 cm^{-1}) increases with increasing the electrolyte content due to the formation of hydrogen bonds with free OH [28].

The sharp peak that appears at 1729 cm^{-1} is assigned to the stretching vibrations of the carbonyl groups (C=O) of 2HPA and vinyl acetate (VAc) monomers [29–31]. This peak is slightly blue-shifted by $\sim$ 2 cm^{-1} and loses intensity with increasing electrolyte content. The peak at 1666 cm^{-1} behaves similarly to the one at 1729 cm^{-1} i.e. blue-shifted by $\sim$ 10 cm^{-1} with reduced intensity with increasing
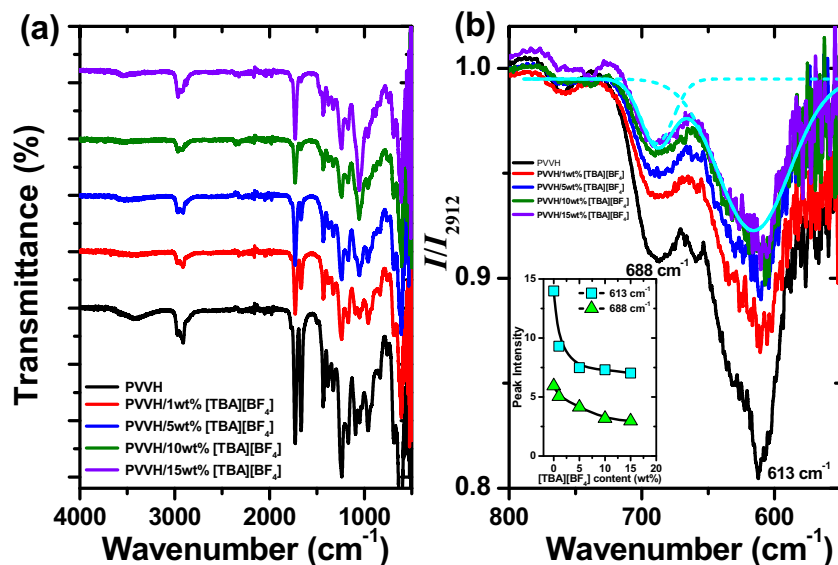
Fig. 1 a ATR-FTIR transmission spectra for pure PVVH (black line) and its composites with [TBA][BF$_4$] weight content of 1 wt% (red line), 5 wt% (blue line), 10 wt% (olive line) and 15 wt% (violet line). **b** The transmittance normalized to the CH$_2$ symmetric stretching band at 2912 cm^{-1}. The two bands at 613 and 688 cm^{-1} are zoomed in **b** and the inset shows the variation of the 613 cm^{-1} (squares) and 688 cm^{-1} (up triangles) peaks intensities with the electrolyte content. The solid cyan line indicates the summation of two Gaussian functions, while the short-dashed lines represent the individual fit for each peak. Solid lines in the inset are guides for the eye

electrolyte concentration. This peak is most probably due to simple hydrolysis of the acetyl groups with the formation of OH [27]. The lower wavenumber peaks at 1435, 1377, and 1234 are related to the CH$_2$, CH$_3$, and C–O vibrations of VAc, while peaks at 1387, 1172, and 1049 cm^{-1} are corresponding to the CH$_3$, O–C=O, and C–O–C vibrations of 2HPA monomers [29, 31].

The remaining vibrations of vinyl chloride (VC) monomers are located at 1426, 1331, 1093, and 613–688 cm^{-1} for CH$_2$, CH, C–C, and C–Cl, respectively [32, 33]. The latter C–Cl stretching bands at 613 cm^{-1} and 688 cm^{-1} are replotted in Fig. 1b after normalizing the ATR spectra to the CH$_2$ symmetric stretching band at 2912 cm^{-1} for a reasonable comparison. It is observed that the two bands are red-shifted by about 5 cm^{-1} accompanied by a substantial reduction in peak intensities with increasing electrolyte concentration as shown in the inset of Fig. 1b. The shift and change in intensity of the two bands are due to the interaction between PVVH terpolymer and the [TBA][BF$_4$] plasticizer. The change of C–Cl peak intensities was reported by Lei et al. for PVVH [8], however, with temperature. They observed a linear increase in the relative intensities of the two bands with increasing temperature.

3.2 Kinetics of thermal degradation

The thermal properties of polymers and their composites give valuable information regarding toughness, stiffness, miscibility with other compounds, and stability. Thermogravimetric analysis (TGA) is usually used to characterize various polymeric materials. Its thermogram displays the weight-decreasing pattern of the materials during thermal decompositions. Differential thermal gravimetric (DTG) curves exhibit the maximum/peak temperature of decomposition at every step of thermal decomposition. In TGA, the mass change of a material is recorded with the temperature at a constant heating rate. In general, two different types of thermal degradation processes are realized in polymeric materials and they are called depolymerization of the chain and random decomposition. The latter occurs by rupturing the chain at random points leading to a dispersed mixture of fragments, while the former is essentially a reverse polymerization process during which monomer units are released from the end of a chain or at a weak linker. Both processes cause the material to lose mass at certain high temperatures.

Figure 2a–f displays the TGA/DTG of PVVH, [TBA][BF$_4$], and their composites in the temperature

range from 23 to 800 °C in steps of 10 °C min^{-1}. The TGA behavior of PVVH can be distinguished into four stages. The first stage (I) is observed in the temperature range ∼ 23 to 214 °C with weight loss of 2.95% and peak temperature (T_P) of 129 °C. This stage is attributed to the evaporation of H_2O and residual solvent. The major chemical reaction in the second stage (II) (218–351 °C) is the dechlorination reaction with the main degradation product of HCl and a small quantity of Cl_2. This stage includes also the elimination of acetic acid at about 250 °C with an overall weight loss of 57.27% and T_P of 277 °C [34–36].

The elimination of HCl and acetic acid will leave behind longer polyene chains and increase the probability of radical propagation and molecular reactions leading to C–Cl bond cleavage [37–39]. At temperatures above 310 °C, the chain radical mechanism becomes relevant and the melting of C–C or C–H bonds occurs [34]. The third degradation step (III) of PVVH is observed between 427 and 483 °C with weight loss of 15.9% and T_P of 446 °C. The fourth

Fig. 2 TGA/DTG measurements for PVVH (a), [TBA][BF$_4$] (f) and their composites with [TBA][BF$_4$] weight content of 2.5 wt% (b), 5 wt% (c), 10 wt% (d) and 20 wt% (e)
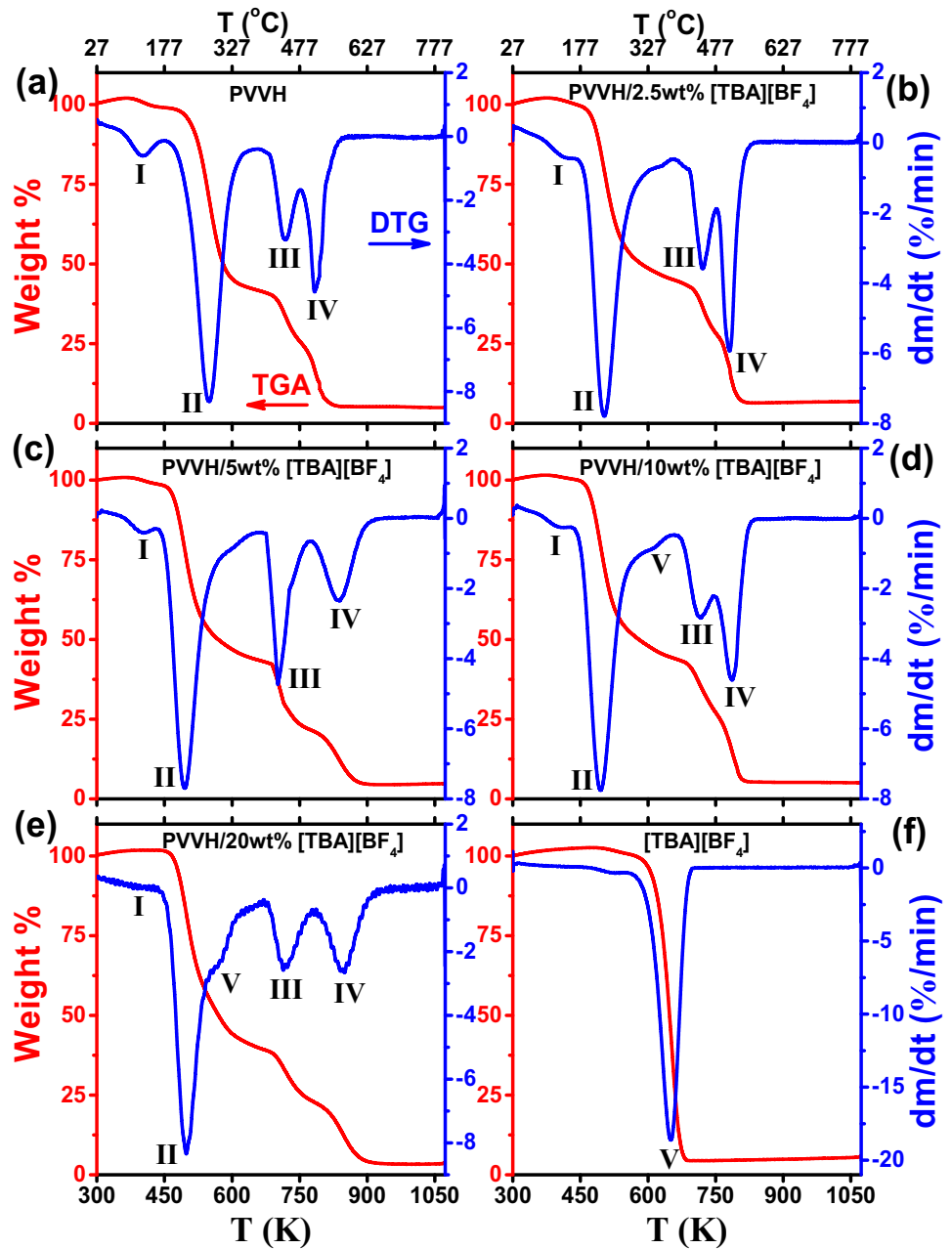
Table 1 TGA/DTG peak temperature (T_p) and the percentage of weight loss (%) for PVVH, [TBA][BF$_4$], and their composites

Sample	Stage I		Stage II		Stage III		Stage IV		Stage V	
	T_p °C (K)	Weight (%)	T_p °C (K)	Weight (%)	T_p °C (K)	Weight (%)	T_p °C (K)	Weight (%)	T_p °C (K)	Weight (%)
PVVH	129 (402)	2.95	277 (550)	57.27	446 (719)	15.9	510 (783)	20.87	–	–
PVVH/1 wt% [TBA][BF$_4$]	141 (414)	4.17	237 (510)	58.86	448 (721)	16.66	537 (810)	21.37	–	–
PVVH/2.5 wt% [TBA][BF$_4$]	150 (423)	2.69	230 (503)	56.95	448 (721)	16.67	509 (782)	21.52	–	–
PVVH/5 wt% [TBA][BF$_4$]	131 (404)	2.18	223 (496)	47.61	429 (702)	14.87	565 (838)	16.41	–	–
PVVH/10 wt% [TBA][BF$_4$]	128 (401)	1.97	222 (495)	57.69	448 (721)	18.48	514 (787)	18.89	319 (592)	–
PVVH/15 wt% [TBA][BF$_4$]	–	–	216 (489)	52.2	443 (716)	12.71	558 (831)	16.19	306 (597)	–
PVVH/20 wt% [TBA][BF$_4$]	–	–	226 (499)	52.6	441 (714)	16.81	557 (830)	18.71	304 (577)	9.96
[TBA][BF$_4$]	–	–	–	–	–	–	–	–	378 (651)	96.93

stage (IV) (491–561 °C) reveals weight loss and T_p of 20.87% and 510 °C, respectively. Thermal degradation of polyene sequences can be executed in the third and fourth stages because the volatile aliphatic and aromatic compounds are produced via the intramolecular cycle of conjugate sequences [40]. From the temperature range of each degradation stage, it is obvious that the second degradation stage is the fastest and most prominent one. Therefore, the kinetics of thermal degradation of this stage will be investigated in more detail as we will see below.

On the other hand, the PVVH/[TBA][BF$_4$] composites display similar behavior of thermal degradation as pure PVVH however with a slight change in weight loss. Surprisingly, the second stage related to dehydrochlorination and removal of acetic acid demonstrates a remarkable reduction in T_p from 277 to 237 °C just by adding 1wt% of [TBA][BF$_4$] plasticizer to PVVH. This reduction continues until reach 216 °C at 15 wt% of [TBA][BF$_4$]. The rapid decrease in T_p with increasing electrolyte concentration is most probably due to the plasticization effect of [TBA][BF$_4$]. Besides reduction in T_p, the composites with high content of electrolyte are decomposed in five stages as shown in Fig. 2d and e. The decomposition of butylammonium ions (Fig. 2f) can be carried out at a high temperature yielding an amine that can interact with HClO$_4$ produced from thermal degradation of PVVH forming amine perchlorate

[17, 41]. Based on the classical Hoffmann degradation of quaternary ammonium salts produces HBF$_4$, which in turn leads to the appearance of HF and BF$_3$ [42]. The peak temperature and percentage of weight loss for all degradation stages for all samples are compiled in Table 1.

The kinetics of the thermal degradation process can be expressed by the theory of activated complexes as follows [43, 44]

$$K = \frac{\gamma e k_B T}{h} \exp\left(\frac{\Delta S}{R}\right) \exp\left(-\frac{E_a}{RT}\right) \qquad (1)$$

Here, K is the degradation rate while k_B, h, and R are the Boltzmann, Planck, and universal gas constants, respectively. ΔS and E_a are the activation of entropy and activation energy of decomposition, respectively, whereas, e (= 2.7183) and T are the coefficient of transmission (unity for monomolecular reaction), Neper number, and the absolute temperature, respectively. Equation (1) is based on the Arrhenius equation as

$$K = f \exp\left(-\frac{E_a}{RT}\right) \qquad (2)$$

where f is the frequency factor that can be expressed as follows

$$f = \frac{\gamma e k_B T}{h} \exp\left(\frac{\Delta S}{R}\right) \qquad (3)$$

Hence, ΔS can be estimated as follows

$$\Delta S = 2.303 \left[\log\left(\frac{fh}{ek_B T}\right)\right] R \qquad (4)$$

and

$$E_a = \Delta H + RT \qquad (5)$$

where ΔH is the activation of enthalpy. Therefore, the Gibbs free energy (ΔH) can be determined as follows

$$\Delta G = \Delta H - T\Delta S \qquad (6)$$

The thermodynamic parameters (E_a, ΔH, ΔS, and ΔG) of each decomposition stage of PVVH and its composites can be estimated graphically by applying the Coats–Redfern method using order of reaction $n = 1$ [45]

$$\log\left[\frac{-\log(1-g)}{T^2}\right] = \log\frac{fR}{\delta E_a}\left[1 - \frac{2RT}{E_a}\right] - \frac{E_a}{2.303RT} \qquad (7)$$

Here, δ is the rate of heating and g is the extent of the reaction for each stage and described by the following equation

$$g = \frac{m_0 - m_i}{m_0 - m_f} \qquad (8)$$

Here, m_0 and m_f are the initial and final/residual masses, respectively, while m_i is the mass at time/temperature i.

For $2RT/E_a \ll 1$, Eq. (7) becomes

$$\log\left[\frac{-\log(1-g)}{T^2}\right] = \log\frac{fR}{\delta E_a} - \frac{E_a}{2.303RT} \qquad (9)$$

A plot of $\log[-\log(1-g)/T^2]$ against $1000/T$ (Fig. 3a–f) will result in a straight line with slope $= -E_a/2.303R$ from which E_a is obtained. On the other hand, the frequency factor f is determined from the intercept of the straight line with the y-axis at $\log fR/\delta E_a$.

The kinetic parameters for dehydrochlorination (HCl removal) and deacetylation (acetic acid removal) of PVVH and its composites are calculated from stage II (Fig. 3a–f) and given in Table 2. The parameters of the olefinic backbone breakage at high temperatures (> 400 °C) are not calculated due to the overlapping between stages III and IV. The activation energy for acids removal (E_a) is found to increase with increasing electrolyte content in PVVH revealing an enhancement of thermal stability for the

composite samples. The value of E_a for pure [TBA][BF$_4$] (~ 194 kJ mol^{-1}) is close to the reported one by Prasad et al. [17] (233 kJ mol^{-1}). The difference between the two values might come from the different heating and gas flow rates. The impact of internal plasticization of VC by the copolymerization with VAc and 2HPA is evident in the low value of E_a (81.51 ± 0.34 kJ mol^{-1}) for PVVH compared to the most recently reported value for PVC (119.8 ± 12.4 kJ mol^{-1}) [46]. The enthalpy and entropy values (Table 2) tell us about the changes in the internal structure or organization during the process of degradation. The negative values of ΔS reveal that the reaction rate is slower than normal.

As seen in Table 2, there is a correlation between E_a and f i.e., a large value of E_a is accompanied by a large value of f and vice versa, a phenomenon often called the compensation or isokinetic effect or θ-rule [47, 48] as shown in Fig. 4a. In addition, a linear relationship is observed between entropy (ΔS) and enthalpy (ΔH) which indicates the direct proportionality between these two quantities as shown in Fig. 4b. The linear relationship between ΔH and ΔS confirms the existence of the compensation phenomenon in PVVH/[TBA][BF$_4$] composites. The compensation effect reveals that the enthalpy variation accompanying the changes in temperature as the molecular cleavage of the polymer occurs during the decomposition process is compensated by the variation in the enthalpy change [48].

The isokinetic temperature (T_{iso}), isokinetic rate constant (k_{iso}), and E_a are correlated by the following expression [47, 48]

$$\ln f = \ln k_{iso} + \frac{E_a}{RT_{iso}} \qquad (10)$$

The isokinetic temperature (T_{iso}) is the temperature at which the chemical reactions proceed at the same rate. At $T > T_{iso}$, faster reactions hold higher activation energies and at $T < T_{iso}$, the faster reactions proceed with lower activation energies. To get T_{iso} and k_{iso} for the composites, a linear fit is made by Eq. (10) to the data points shown in Fig. 4a. The fit produces the following expression $\ln f = -10.14551(\pm 2.03702) + 0.27072(\pm 0.02104)E$ with slope ($= 1/RT_{iso}$) and intercepts ($= \ln k_{iso}$) of 0.27072 and -10.14551, respectively. The latter gives k_{iso} of 3.93×10^{-5} s^{-1} while the former gives T_{iso} of 444.3 K. Similarly, the linear fit of ΔH–ΔS (Fig. 4b) gives an analogous expression $\Delta S = -0.33276$

Fig. 3 Coats–Redfern (C-R) plots for thermal degradation of stage II for PVVH (**a**), [TBA][BF$_4$] (inset of (**f**)) and their composites with [TBA][BF$_4$] weight content of 1 wt% (**b**), 5 wt% (**c**), 10 wt% (**d**), 15 wt% (**e**) and 20 wt% (**f**). Linear fits (solid lines) give the activation energy of decomposition (E_a) and the frequency factor (f) (see Table 2)
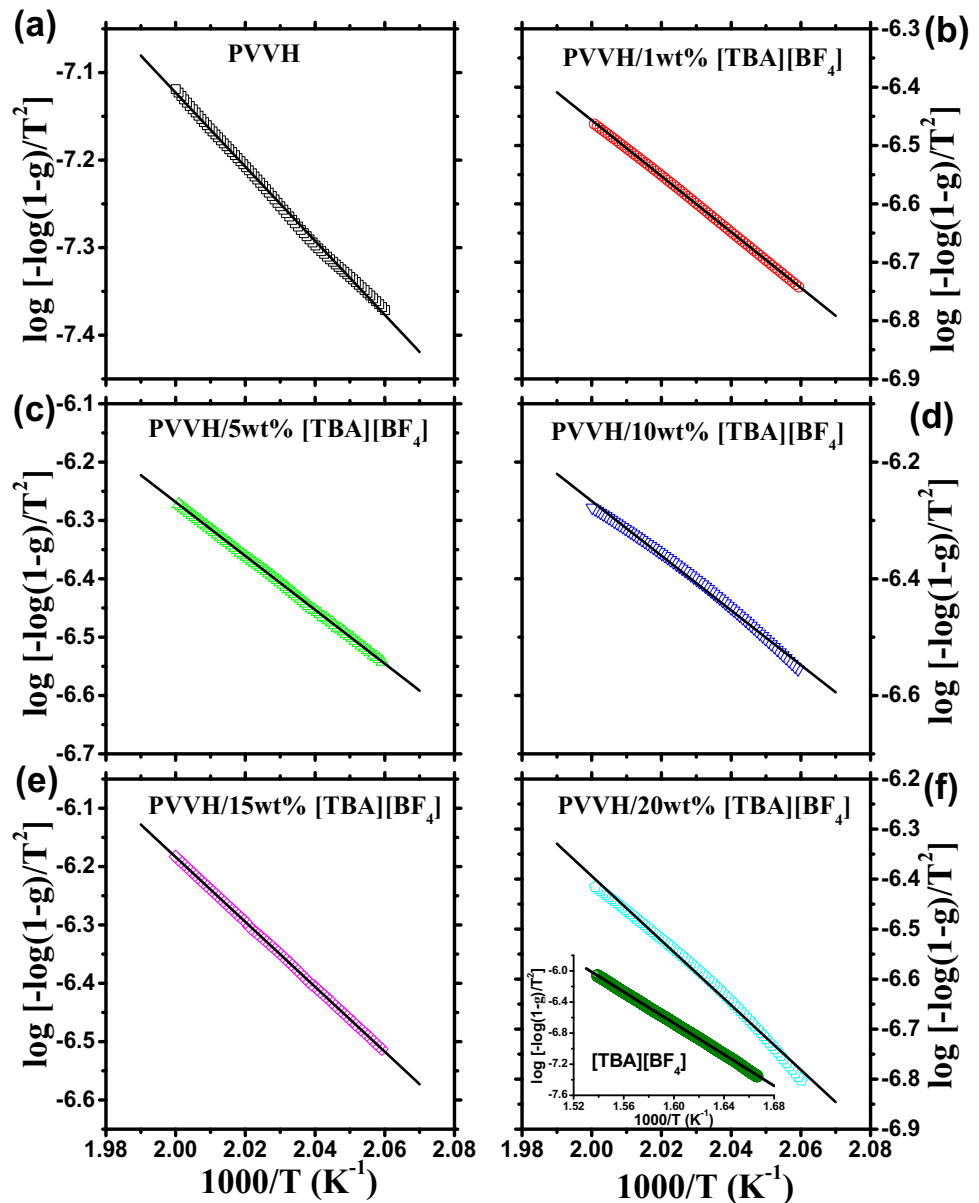

Table 2 C–R kinetic parameters for PVVH, [TBA][BF$_4$], and their composites

Sample	E_a (kJ mol^{-1})	f (s^{-1})	ΔH (kJ mol^{-1})	ΔS (kJ mol^{-1} K^{-1})	ΔG (kJ mol^{-1})
PVVH	81.05 ± 0.37	3.58 × 10^4	76.94	− 0.171	170.62
PVVH/1 wt% [TBA][BF$_4$]	91.68 ± 0.14	2.42 × 10^6	86.39	− 0.136	156.55
PVVH/2.5 wt% [TBA][BF$_4$]	90.06 ± 0.55	2.26 × 10^6	86.36	− 0.136	154.26
PVVH/5 wt% [TBA][BF$_4$]	88.43 ± 0.11	1.65 × 10^6	86.31	− 0.138	152.98
PVVH/10 wt% [TBA][BF$_4$]	89.63 ± 0.69	2.24 × 10^6	85.23	− 0.136	152.79
PVVH/15 wt% [TBA][BF$_4$]	106.53 ± 0.08	1.88 × 10^8	104.46	− 0.099	150.86
PVVH/20 wt% [TBA][BF$_4$]	123.67 ± 1.11	8.31 × 10^9	119.04	− 0.067	153.27
[TBA][BF$_4$]	194.17 ± 0.04	1.39 × 10^{13}	188.76	− 0.008	194.02

Fig. 4 **a** Activation energy (E_a)-frequency factor (*f*) compensation plot. **b** Enthalpy (ΔH)–entropy (ΔS) compensation plot
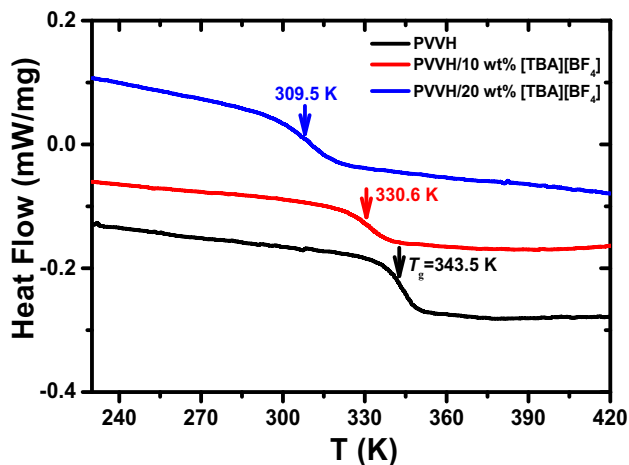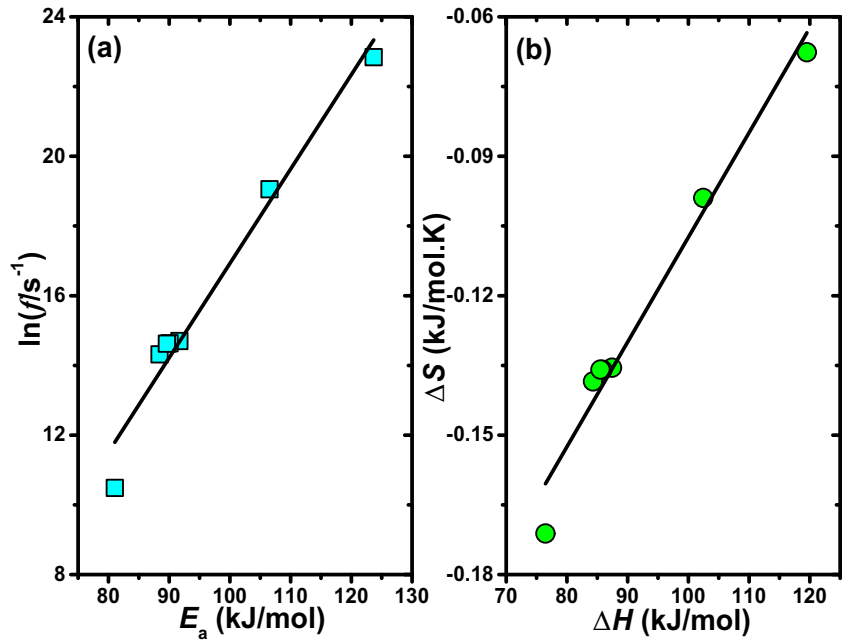

Fig. 5 DSC traces for pure PVVH (black line) and PVVH/[TBA][BF$_4$] composites with [TBA][BF$_4$] weight content of 10 wt% (red line) and 20 wt% (blue line) measured on cooling from 473 to 223 K with a cooling rate of 10 °C min^{-1}. The downward vertical arrows give the locations of T_g for PVVH and the corresponding composites

$(\pm 0.01598) + 0.00225(\pm 1.72467 \times 10^{-4})\Delta H$. Values in brackets represent the error limit.

The compensation effect of PVVH and PVVH/PMMA blend was reported using thermally stimulated depolarization current (TSDC) and found a T_{iso} of 352 K [22, 49]. Thermal degradation of PVC and PVAc and their blends were investigated by Sivalingam et al. [33] using TGA. They reported T_{iso} of

533 and 716 K for the acid and olefinic removal, respectively, for PVC degradation with the corresponding k_{iso} of 4.9×10^{-4} and 2.3×10^{-4} s^{-1}. On the other hand, the PVAc demonstrated T_{iso} of 583 and 709 K with k_{iso} of 6.9×10^{-4} and 2.1×10^{-4} s^{-1}, for acetic acid and olefinic removal, respectively. They concluded from their study that after the removal of HCl and acetic acid the backbone of both polymers is identical and therefore will have the same stage of degradation.

The effect of plasticization of PVVH by the addition of electrolyte is also evident in the reduction of T_g for PVVH from ~ 344 K to 310 with increasing [TBA][BF$_4$] concentration from 10 to 20 wt% as shown in Fig. 5. Plasticization causes a change in the PVVH conformation by reducing the inter- and intramolecular interaction maintaining the flexibility of the polymer backbone to bend and slide more readily.

Based on the DSC results, one can assume that [TBA][BF$_4$] electrolyte acts as an external plasticizer for PVVH that is internally plasticized by the copolymerization of VC with VAc and 2HPA monomers to reduce the T_g of VC from 355 to 344 K. Further reduction in T_g from 344 to 310 K is achieved by adding [TBA][BF$_4$] to PVVH. Two conceivable scenarios for PVVH plasticization by [TBA][BF$_4$]. The first scenario is based on the lubrication theory in which plasticizer molecules minimize segment–segment interaction of PVVH and consequently keep the

Fig. 6 a Absorbance against wavelength (λ) and **b** Absorption coefficient (α) against incident photon energy ($h\nu$) for pure PVVH and PVVH/[TBA][BF$_4$] composite samples. Short dashed lines in **b** represent the fit of the linear part of the plot
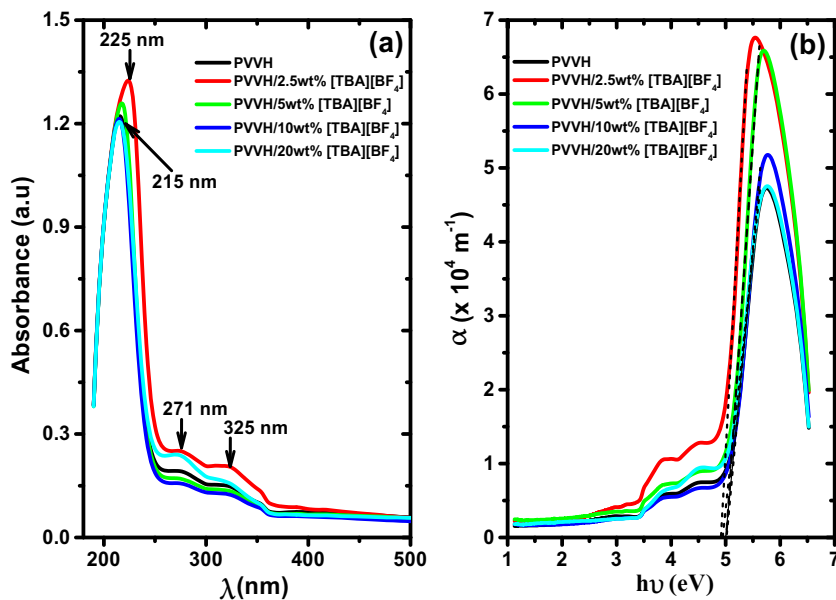
polymer chains apart and maintain flexibility. Furthermore, it can act as a lubricant that allows the PVVH chains to slide over each other. The second scenario is based on the free volume theory in which polymer chains are closely packed and restricted in motion in the glassy state. Heating the polymer above T_g creates more free volume which is occupied by the plasticizer resulting in lowering T_g by separating PVVH chains [50]. The spectacular reduction in T_g of PVC due to external and internal plasticizers has been reported by many researchers [51–55]. For example, Li et al. [53] incorporated four plasticizers into the PVC chain via a glutamic acid linker and found a strong depression of T_g for PVC-triethylene glycol esters compared to PVC-alkyl esters. Moreover, they found a correlation between the plasticizer length and T_g i.e., longer length plasticizer correlates with lower T_g. In addition, TGA measurements for these compounds demonstrated that the PVC-triethylene glycol esters degrade at lower temperatures than the PVC-alkyl esters. Navarro et al. [56] have used trichlorotriazine (TCTA)-based sodium thiolates with different aliphatic chains as an external plasticizer that is covalently bonded with PVC. They observed a reduction in T_g below 0 °C when commercial polyether amines, terminated Jeffamines, and polypropylene glycol were used. Similar results were reported by the same group for the conventional PVC-di-2-ethyl hexyl phthalate blends [57].

3.3 UV–Vis spectroscopy

The absorption spectra of PVVH and its composites were recorded in the wavelength (λ) range 190–1100 nm and displayed in Fig. 6a. Pure PVVH demonstrates three absorption peaks at 215, 271, and 325 nm [25]. The fast peak at 215 nm is related to the $n \rightarrow \pi^*$ transition while the other two peaks at 271 and 325 nm are due to the $\pi \rightarrow \pi^*$ transition between the unsaturated bond of the carbonyl groups (C=O) that was monitored in the ATR-FTIR at 1729 cm^{-1}. The PVVH peak at 215 nm is shifted to 225 nm and gains intensity just by adding 2.5 wt% of the electrolyte and returning to its initial position at 20 wt%. The other two peaks (271 and 325 nm) are slightly shifted to lower wavelengths up on the addition of the electrolyte.

The exponential increase in absorption coefficient α (= 2.303A/d, A: absorbance, and d: sample thickness) with incident photon energy ($h\nu$) is the main characteristic of absorption edge (E_{edge}) that is related to severe discontinuity in the absorption spectrum when the absorbed photon energy matches an electronic transition. The absorption edge (E_{edge}) is estimated by fitting the linear part of the α–$h\nu$ plot (Fig. 6b) and then extrapolating the fitting line to $\alpha = 0$. The values of E_{edge} are slightly changing with increasing the electrolyte content in the PVVH matrix (Table 3).

Table 3 The optical parameters for PVVH/[TBA][BF$_4$] composite samples

Optical parameters	Pure PVVH	PVVH/2.5 wt% [TBA][BF$_4$]	PVVH/5 wt% [TBA][BF$_4$]	PVVH/10 wt% [TBA][BF$_4$]	PVVH/20 wt% [TBA][BF$_4$]
E_{edge} (eV)	4.99 ± 0.38	4.92 ± 0.42	5.01 ± 0.44	5.02 ± 0.30	4.94 ± 0.34
E_U (eV)	2.25 ± 0.04	1.63 ± 0.03	3.33 ± 0.16	2.27 ± 0.08	4.10 ± 0.28
β	0.012	0.016	0.010	0.012	0.006
$E_{g\text{-direct}}$ (eV) (Region II)	5.22 ± 0.43	5.11 ± 0.64	5.23 ± 0.50	5.24 ± 0.65	5.19 ± 0.31
$E_{g\text{-direct}}$ (eV) (Region I)	3.33 ± 0.33	3.34 ± 0.23	3.29 ± 0.22	3.34 ± 0.17	3.40 ± 0.27
$E_{g\text{-indirect}}$ (eV) (Region II)	4.72 ± 0.12	4.66 ± 0.25	4.77 ± 0.19	4.75 ± 0.17	4.66 ± 0.14
$E_{g\text{-indirect}}$ (eV) (Region I)	2.41 ± 0.11	2.44 ± 0.07	2.23 ± 0.11	2.27 ± 0.14	2.53 ± 0.12
ε_L	2.98 ± 0.01	3.32 ± 0.03	2.65 ± 0.02	2.54 ± 0.02	2.66 ± 0.02
N/m^* ($\times 10^{67}$ m^{-3} kg^{-1})	3.58	5.19	2.15	1.72	2.89
ω_p ($\times 10^{20}$ rad s^{-1})	3.22	3.88	2.49	2.23	2.90
E_0 (eV)	4.46 ± 0.07	4.37 ± 0.13	4.60 ± 0.06	4.54 ± 0.09	4.34 ± 0.09
E_d (eV)	3.02 ± 0.05	3.61 ± 0.11	3.31 ± 0.05	2.91 ± 0.06	2.62 ± 0.06
F (eV)^2	13.45 ± 0.29	15.77 ± 0.67	15.22 ± 0.30	13.19 ± 0.38	11.37 ± 0.35
M_{-1}	0.676 ± 0.015	0.826 ± 0.035	0.720 ± 0.014	0.638 ± 0.018	0.604 ± 0.018
M_{-3}, (eV)$^{-2}$	0.034 ± 0.002	0.043 ± 0.004	0.034 ± 0.001	0.031 ± 0.002	0.032 ± 0.002
n_0	1.295 ± 0.006	1.351 ± 0.013	1.312 ± 0.005	1.280 ± 0.007	1.267 ± 0.007
ε_s	1.676 ± 0.015	1.826 ± 0.035	1.720 ± 0.014	1.638 ± 0.018	1.604 ± 0.018
η ($\times 10^{-37}$ C^2 m^2 J^{-1})	1.94	2.28	2.04	1.85	1.77
η' ($\times 10^{-27}$ m^3)	1.74	2.05	1.83	1.66	1.59
λ_0 ($\times 10^{-7}$ m)	2.78	2.84	2.70	2.73	2.86
s_o ($\times 10^{12}$ m^{-2})	8.75	10.26	9.90	8.58	7.40
$\chi^{(1)}$	0.054 ± 0.001	0.066 ± 0.003	0.057 ± 0.001	0.051 ± 0.002	0.048 ± 0.002
$\chi^{(3)}$ ($\times 10^{-15}$ e.s.u.)	1.50	3.34	1.93	1.19	0.96
n_2 ($\times 10^{-14}$ e.s.u)	4.37	9.33	5.54	3.52	2.85

The width of band tail or Urbach tail energy (E_U) can be estimated from the exponential dependence of α–hv relation [58, 59]

$$\alpha = \alpha_0 \exp\left(\frac{hv}{E_U}\right) \tag{11}$$

Here, α_0 is the pre-exponential factor. Figure 7a shows the Lnα–hv linear relationship for all samples. The linear fit of data points gives E_u-values between ∼ 1.63 and 4.1 eV (Table 3). The increase of E_u with electrolyte concentration can be interpreted by the fact that an increase in electrolyte content may lead to defects and imperfections in the amorphous structure of PVVH, a condition that may increase localized states within the forbidden gap. Our results are consistent with previous work for PVVH filled with cobalt chloride [24].

The calculated values of E_U can be used to get the steepness parameter (β) (Table 3) that characterizes the broadening of E_{edge} due to electron/exciton–photon interaction according to the following relation

$$\beta = \frac{k_B T}{E_U} \tag{12}$$

Here, T (= 300 K) is the absolute temperature and k_B is the Boltzmann constant.

The optical characterization of materials is generally governed by the interaction between the materials and the electric field of incident electromagnetic waves. The behavior of the extinction coefficient k (= $\alpha\lambda/4\pi$) with the wavelength gives a reasonable indication of the certainty that these interactions have taken place, and thus, it describes the propagation and velocity of the electromagnetic wave through the materials. Figure 7b depicts the variation of k with wavelength for PVVH/[TBA][BF$_4$] composite samples. The behavior of all samples demonstrates a significant decrease in k values as λ increases

Fig. 7 a Ln α against incident photon energy (*hv*) and **b** Extinction coefficient (*k*) against wavelength (*λ*) for pure PVVH and PVVH/ [TBA][BF$_4$] composite samples
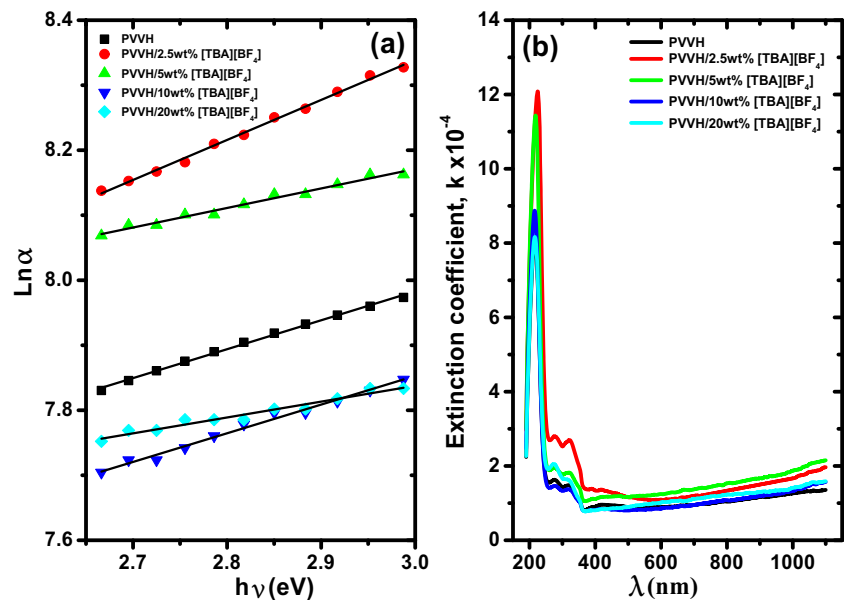
from ∼ 215 to 500 nm followed by an increase at longer wavelengths. Furthermore, the composites exhibit higher *k* values compared to the pristine PVVH. The decrease in *k* values confirms that these materials allow electromagnetic waves to pass through without any damping or decay in this region. On the other hand, the increase of *k* at higher wavelengths indicates to more scattering of photons is taking place with increasing [TBA][BF$_4$] in the PVVH matrix. Similar behavior has been found for amorphous semiconductors [60].

The optical energy gap (*E$_g$*) is an essential parameter for determining the amount of absorbed solar spectrum by a photovoltaic cell. It is the difference in energy between the top and bottom of the valence and conduction bands, respectively. The *E$_g$*, α, and *hv* are interrelated through the Tauc equation [61]

$$\alpha h\upsilon = B(h\upsilon - E_g)^x \tag{13}$$

where *B* is the band tail parameter and the index *x* identifies the type of electronic transition. The latter takes 1/2 (direct) and 2 (indirect) for allowed transitions while forbidden transitions are given *x*-values of 3/2 (direct) and 3 (indirect), respectively. The predominant transitions in our case are the allowed direct and indirect transitions with two optical energy gaps. The onset optical gap (region I) is corresponding to the onset of optical absorption and formation of abound electron–hole pair or exciton. On the other hand, the second optical gap (region II) is a fundamental gap (HOMO-LOMO) that

corresponds to the minimum energy formation of separated, uncorrelated free electrons and holes [62, 63]. Extrapolating the linear fitted parts of Fig. 8a and b to $(\alpha h\upsilon)^{0.5}$ and $(\alpha h\upsilon)^2 = 0$ will give the values of direct (*E$_{g\text{-direct}}$*) and indirect (*E$_{g\text{-indirect}}$*) *E$_g$* for the onset and fundamental energy gaps of PVVH and its composites (Table 3). An insignificant decrease in *E$_{g\text{-direct}}$* and *E$_{g\text{-indirect}}$* is observed with increasing the content of electrolytes in the PVVH matrix. Furthermore, the *E$_{g\text{-indirect}}$* values are less than the *E$_{g\text{-direct}}$* ones by about 0.5 eV. The slight variation in *E$_g$* with electrolyte concentration could be explained based on the fact that incorporating small amounts of doping would form charge-transfer complexes (CTCs) in the PVVH network leading to an increase in optical conductivity and variations in the *E$_g$* by giving additional charges to the network [64].

Investigating the refractive index (*n*) for the performance of optical systems is very important and necessary to match or optimize the numerical aperture of the optical reduction system at all points in an optical path. The refractive index control of optical polymers makes it suitable for a wide range of industrial and medical applications such as optical communications, anti-reflective coatings, light-emitting diodes, organic solar cells, and polymer lenses. Reflectance (*R*), transmittance (*T*), and *n* are related to each other through the following relation [65].

Fig. 8 a $(\alpha h\upsilon)^{0.5}$ versus $h\upsilon$ (indirect allowed transition) and **b** $(\alpha h\upsilon)^2$ versus $h\upsilon$ (direct allowed transition) for PVVH and PVVH/[TBA][BF$_4$] composite samples. For clarity reasons, the first region of **b** (Region I) is enlarged and presented in the inset
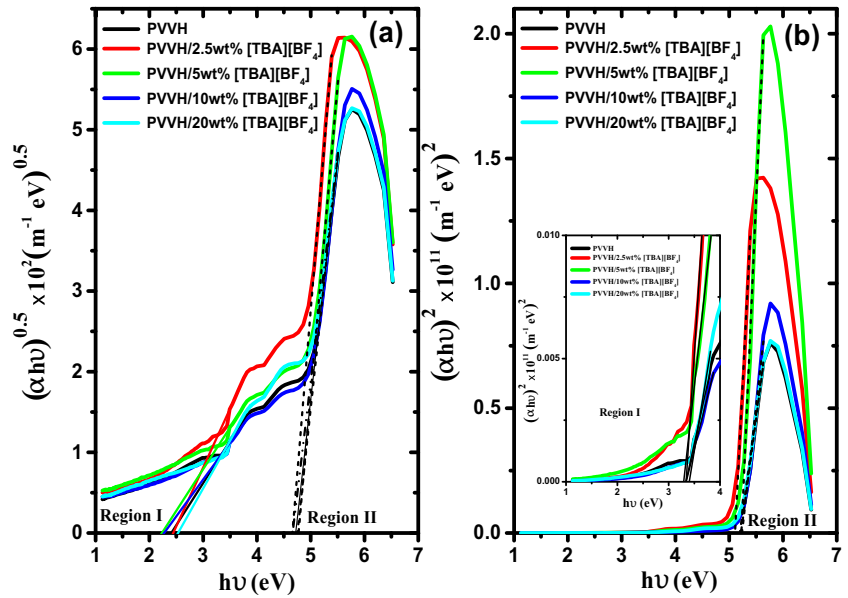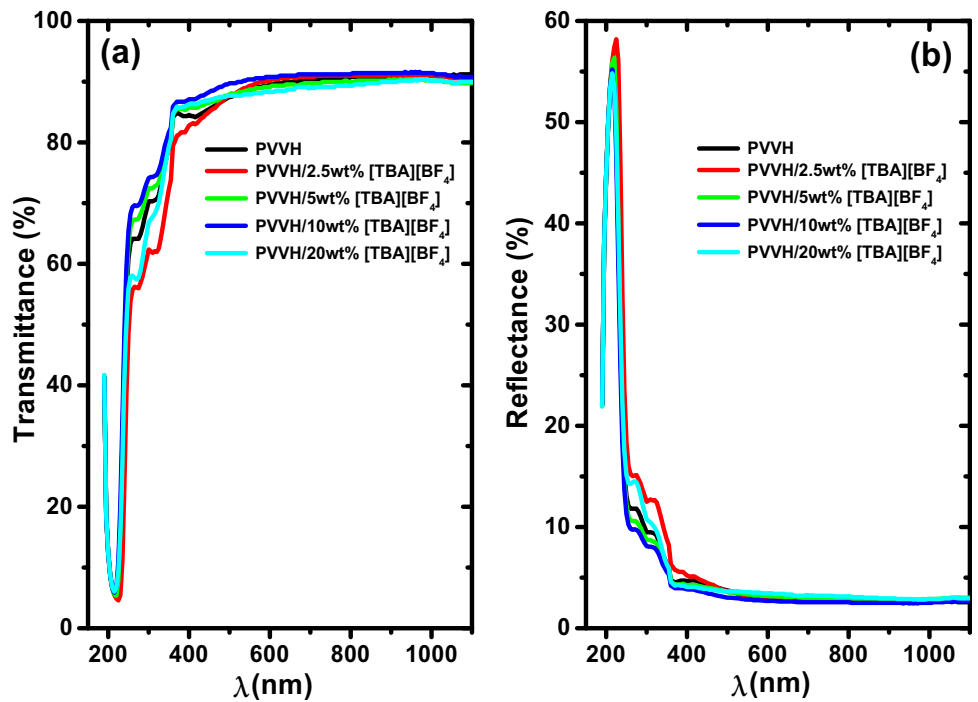

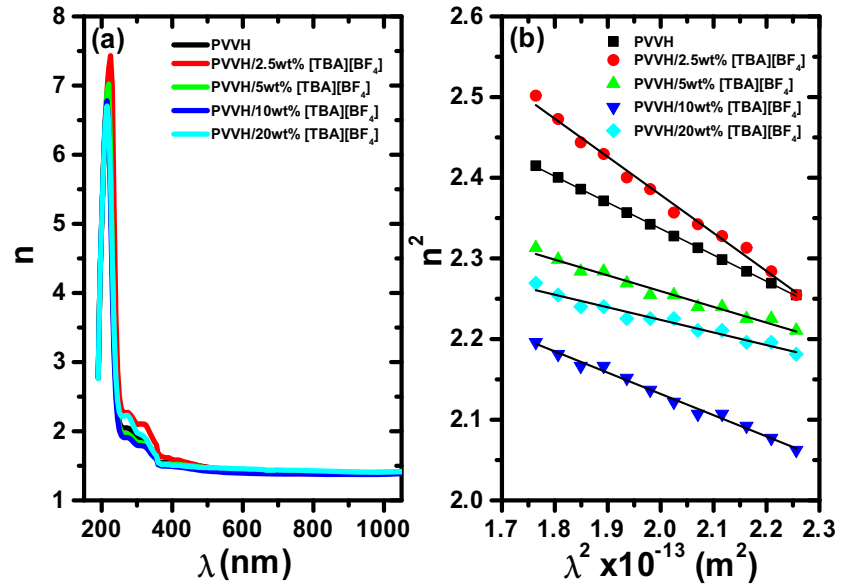**Fig. 9** The transmittance (**a**) and reflectance (**b**) versus wavelength (λ) for pure PVVH and PVVH/[TBA][BF$_4$] composite samples

$$n = \frac{1 + \sqrt{R}}{1 - \sqrt{R}}, \quad R = 1 - \sqrt{Te^A} \quad (14)$$

Figure 9a shows that pure PVVH is an optically transparent material in the visible region with a transmittance exceeding 90%. In addition, it allows the transmission of UV rays by only 5%. The PVVH/[TBA][BF$_4$] composite samples demonstrate similar behavior, however, with lower values. The decrease in transmittance with increasing electrolyte content may be related to the fact that [TBA][BF$_4$] electrolyte acts as scattering centers in the PVVH matrix. On the other side, the reflectance (Fig. 9b) shows an opposite trend to transmission i.e., it screens the UV radiation by 58% and the visible rays by 3%. Furthermore, it increases with increasing electrolyte content. The

Fig. 10 **a** The refractive index (n) versus wavelength (λ) for pure PVVH and PVVH/[TBA][BF$_4$] composite samples. **b** Corresponding plot for n^2 versus λ^2

variations in both the transmittance and reflectance with increasing [TBA][BF$_4$] content in the composite samples may be interpreted using the proportional relationship between free carrier absorption in the polymer material and the number of carriers. As the number of carriers increases, their absorption in the visible and UV regions subsequently increases.

Figure 10a shows the dependence of the refractive index on wavelength. It is observed that the refractive index of all samples decreases with increasing wavelength until a wavelength of 500 nm, after which the refractive index is almost unchanged. The relation between n and λ can be expressed as follows [26]

$$n^2 = \varepsilon_L - \frac{e^2}{\pi c^2}\left(\frac{N}{m^*}\right)\lambda^2 \qquad (15)$$

where ε_L, e, c, and (N/m^*) are the lattice dielectric constant, electronic charge, light speed, and carrier concentration to effective mass ratio, respectively. Figure 10b shows the variation of n^2 versus λ^2 for all samples. The linear fit of experimental data will give the values of ε_L and N/m^* from which the plasma frequency (ω_p) is calculated based on the following equation [66]

$$\omega_p^2 = \frac{e^2}{\varepsilon_0}\left(\frac{N}{m^*}\right) \qquad (16)$$

where ε_0 is the permittivity of free space. Except for 2.5 wt% [TBA][BF$_4$], the values of ε_L, N/m^* and ω_p

(Table 3) are less than the corresponding values of pure PVVH, and at the same time show slight dependence on the electrolyte concentrations.

The refractive index dispersion in PVVH/[TBA][BF$_4$] composite samples can be modeled by the single effective oscillator model proposed by Wemple to get the dispersion energy parameters E_d and E_0 according to the following relation [67]

$$\left(n^2 - 1\right)^{-1} = \frac{E_0}{E_d} - \frac{(h\upsilon)^2}{E_o E_d} \qquad (17)$$

Here, E_d is the energy of dispersion, which is a measure of the strength of the oscillator or average strength of inter-band optical transitions and E_0 is the average excitation energy or the energy of a single oscillator for the electronic transition, respectively. Figure 11 demonstrates the relation between $(n^2 - 1)^{-1}$ and $(h\upsilon)^2$ for all samples. The values of E_0 and E_d are obtained from the intercept and slope of the linear fit to the data points and summarized in Table 3.

The calculated values of E_d and E_0 are used to get several optical parameters as the moments of the imaginary part of the optical spectrum (M_{-1} and M_{-3}), static refractive index (n_0), static dielectric constant (ε_s), and the optical oscillator strength F according to the following equations [67–69]

$$E_0^2 = \frac{M_{-1}}{M_{-3}} \text{ and } E_d^2 = \frac{M_{-1}^3}{M_{-3}} \qquad (18)$$

Fig. 11 **a** $(n^2 - 1)^{-1}$ versus $(hv)^2$ and **b** $(n^2 - 1)^{-1}$ versus (λ^{-2}) for pure PVVH and PVVH/[TBA][BF$_4$] composite samples. Solid lines represent the linear fit to data points
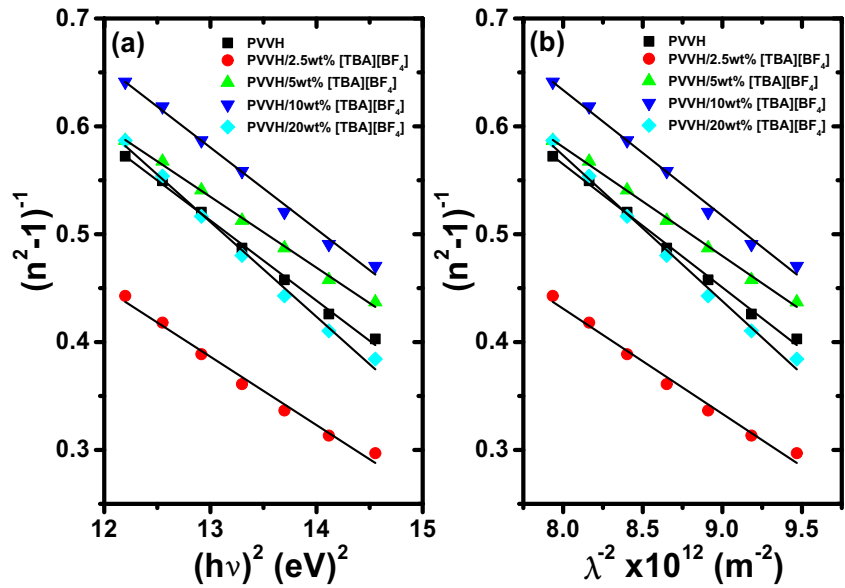
$$n_0 = \left(1 + \frac{E_d}{E_0}\right)^{0.5}, \; \varepsilon_s = n_0^2, \text{ and } F = E_0 E_d \quad (19)$$

The values of ε_s are lower than the corresponding ones for ε_L (Table 3). This difference can be attributed to the contribution of the polarization process that occurs inside the material when light falls on it as well as the increase in the concentration of free carriers. Moreover, the increase in the electrolyte content leads to an increase in the optical oscillator strength F (see Table 3), which means an increase in photon absorption by electrons between the initial and final states.

The molecular polarizability (η) and polarizability volume (η') of PVVH/[TBA][BF$_4$] composite samples can be estimated from the Clausius–Mossotti relation [70]

$$\eta = \frac{3M\varepsilon_0}{\rho N_A} \frac{(\varepsilon_s - 1)}{(\varepsilon_s + 2)} \text{ and } \eta' = \frac{\eta}{4\pi\varepsilon_0} \quad (20)$$

Here, M (= 33,000 g mol^{-1}), ρ (= 1.38 g cm^{-3}) and N_A are the molecular weight, density, and Avogadro's number. The values of η and η' (Table 3) increase with increasing the content of [TBA][BF$_4$]. It is known that electronic polarizability is related to the molecular size and symmetry of a molecule i.e., polarizability volume increases with increasing molecular volume [71]. Adding [TBA][BF$_4$] to PVVH in different concentrations leads to an increase in molecular size and subsequently an increment of polarizability volume (η'). The polarizability volume

of [BF$_4$] has been reported using ab initio-based methods such as HF and MP2 and found η' of 3.495×10^{-30} m^3 [71]. The η' of [BF$_4$] was also estimated optically using UV–Vis spectroscopy and found a value of 4.27×10^{-29} m^3 [26]. Both values are in good agreement with our results.

The dispersion equation can be expressed in terms of the single-term oscillatory model as the following [72]

$$\frac{1}{n^2 - 1} = \frac{1}{(n_0^2 - 1)} - \frac{1}{S_0}\frac{1}{\lambda^2} \text{ and } S_0 = \frac{(n_0^2 - 1)}{\lambda_0^2} \quad (21)$$

where S_0 and λ_0 are the average oscillator strength and the average inter-band oscillator wavelength, respectively. These optical parameters (S_0, λ_0) are calculated from the linear fit of the linear relationship between $(n^2 - 1)^{-1}$ and $1/\lambda^2$ (Fig. 11b and Table 3). The value of S_0 jumps from 8.75×10^{12} to 10.26×10^{12} m^{-2} just by adding 2.5 wt% [TBA][BF4] to PVVH indicating a higher absorption probability in transitions between energy levels.

3.3.1 Nonlinear optical parameters

Sufficient and intense illumination of the material causes a nonlinear response of polarization density to the electric field of light. Determining the nonlinear optical parameters of materials is vital for the fabrication of optical switching and frequency conversion devices, which are an important part of integrated photonics. Third-order nonlinear optical
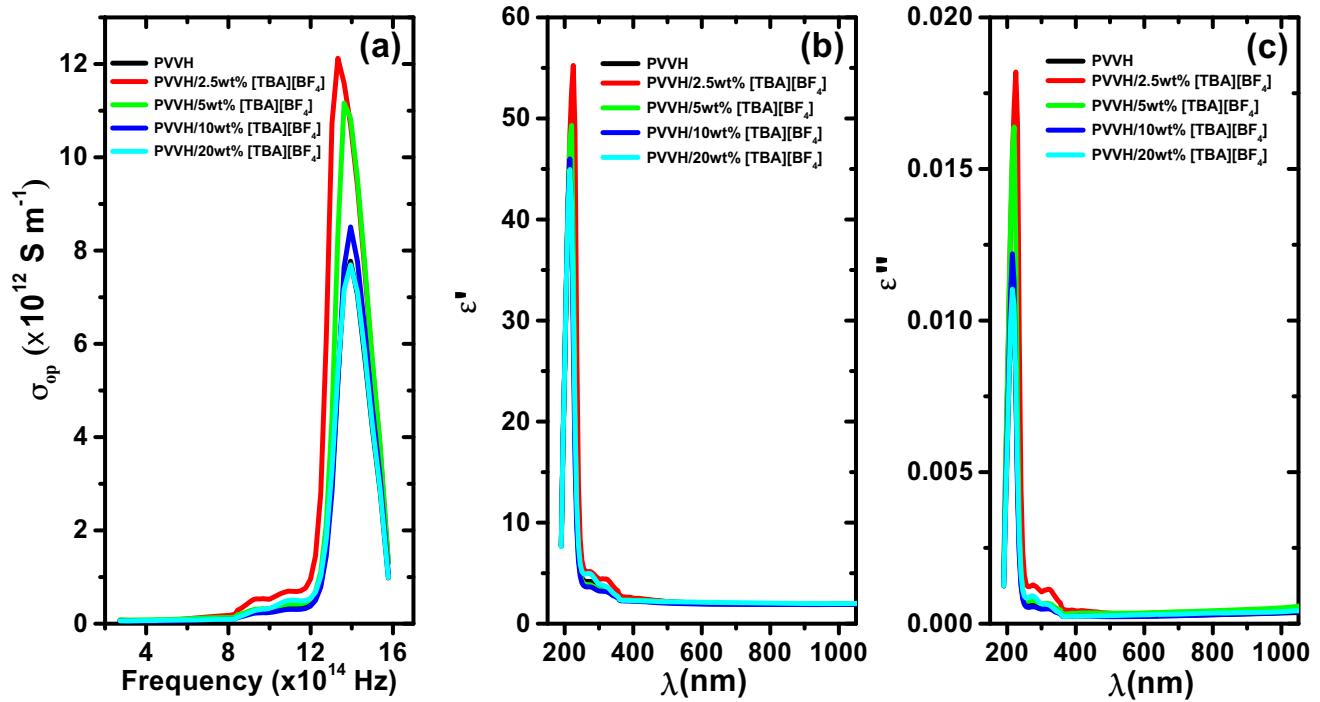
Fig. 12 **a** Optical conductivity (σ_{op}) versus frequency, **b** dielectric constant (ε') versus wavelength, and **c** dielectric loss (ε'') versus wavelength for pure PVVH and PVVH/[TBA][BF$_4$] composite samples

susceptibility ($\chi^{(3)}$) is taken into consideration as a very important nonlinear optical parameter for many applications such as telecommunication systems with high capacities [73]. According to Miller's rule, $\chi^{(3)}$ can be estimated using the following equation [74, 75]

$$\chi^{(3)} = A\left(\chi^{(1)}\right)^4 \qquad (22)$$

where A (= 1.79×10^{-10} esu) is a constant and $\chi^{(1)}$ $\left(= E_d/4\pi E_0\right)$ is the linear optical susceptibility. Therefore, $\chi^{(3)}$ can be expressed as [75]

$$\chi^{(3)} = A\left(\frac{E_d}{4\pi E_0}\right)^4 = \frac{A}{(4\pi)^4}\left(n_0^2 - 1\right)^4 \qquad (23)$$

The values of $\chi^{(3)}$ and n_0 (Table 3) are used to calculate the nonlinear refractive index (n_2) according to the following relation [75]

$$n_2 = \frac{12\pi}{n_0}\chi^{(3)} \qquad (24)$$

The values of n_2 for composites are higher than the corresponding value of pristine PVVH indicating that PVVH/[TBA][BF$_4$] composites could be an excellent candidate for nonlinear optical applications, especially for 2.5 and 5 wt% [TBA][BF$_4$].

3.3.2 Optical conductivity and optical dielectric constant

Figure 12a evince the frequency dependence of optical conductivity $\sigma_{op}(= nc\alpha/4\pi$ [66]) for pure PVVH and PVVH/[TBA][BF$_4$] composite samples. It is obvious from the plot that σ_{op} increases with increasing both frequency and electrolyte concentration. The increase of the latter leads to an increase in the number of charge carriers in the composites and subsequently an increase in σ_{op} and a slight decrease in E_g. One possible reason for the increment of σ_{op} is that [TBA][BF$_4$] electrolyte is fitted well in between the spaces of the PVVH matrix creating a segregated network that increases σ_{op} [76]. On the other hand, the lower values of σ_{op} at lower frequencies may be due to the low availability of mobile charge carriers to transport from one localized state to another because of the interfacial polarization effect in this frequency region. With increasing frequency, the average displacement of the charge carrier decreases, and the conductivity will increase [77].

The real $\left(\varepsilon' = n^2 - k^2\right)$ and imaginary $(\varepsilon'' = 2nk)$ parts of the complex dielectric function $(\varepsilon^* = \varepsilon' - i\varepsilon'')$ for PVVH and its composites are displayed in

Fig. 12b and c as a function of wavelength. Both ε' and ε'' have the same trend with λ and electrolyte concentration but with different values. They increase with increasing the electrolyte content and decrease with increasing λ. It is known that the energy density u (= $1/2\varepsilon_0\varepsilon'E_b$, E_b is the breakdown strength [78]) of a material is directly proportional to its dielectric constant (ε'). That means the PVVH composites achieve higher energy densities than the corresponding pristine PVVH. Similar behavior was recently reported for polymer/ceramic composites [78].

The behavior of ε' exhibit also a wide dispersion region below 500 nm due to the polar nature of composites that follows the fluctuations of the incidental electric field. This dispersion region plays a vital role in the design of optical devices as well as in optical communication. On the other hand, at higher wavelengths, the molecules cannot follow the incident field fluctuations due to the inertia and therefore ε' is almost constant.

The higher values of dielectric loss (ε'') at lower frequencies (Fig. 12c) are due to dipolar polarization. The dipoles in the polymeric material at lower and intermediate frequencies can easily be polarized under the external electric field that displaces the charges from their equilibrium position or traps [79].

4 Conclusion

Composites of PVVH and [TBA][BF$_4$] electrolytes were prepared by casting method. The interaction between the two compounds was traced by ATR-FTIR and found a shift and reduction in the intensity of the C–Cl peaks located at 613 and 688 cm^{-1} due to the interaction between PVVH terpolymer and the [TBA][BF$_4$] plasticizer. The TGA/DTG thermal degradation of the second stage revealed a remarkable reduction in peak temperature (T_p) with increasing electrolyte content due to the dehydrohalogenation and removal of acetic acid. The fast reduction in T_p suggests that [TBA][BF$_4$] electrolyte promotes the removal of hydrogen halide and acetic acid. The glass transition temperature (T_g) of PVVH decreased by 34 K as the electrolyte concentration increased by 20 wt% indicating the plasticization effect of the electrolyte. The possible reason for the reduction in T_g is that the electrolyte changes the PVVH conformation by reducing the inter-and intramolecular interaction maintaining the flexibility of the polymer backbone to bend and slide more readily. The linear correlation between activation energy and frequency factor indicates that these composites demonstrate a compensation effect with k_{iso} and T_{iso} of 3.93×10^{-5} s^{-1} and 444.3 K, respectively.

The UV–Vis measurements for pure PVVH and its composites revealed a transmittance of about 91% for visible light and 5% for UV radiation. The reflectance showed an opposite trend to transmission i.e., it reflected the UV radiation by 58% and the visible rays by 3%. The variation of the optical energy gap with electrolyte content was owed to the formation of charge-transfer complexes by the dopant that increases the optical conductivity (σ_{op}) by giving additional charges to the polymer matrix. Also, the real (ε') and imaginary (ε'') parts of the complex dielectric function were found to decrease with increasing wavelength. Linear and nonlinear optical parameters were estimated and discussed in terms of the single-term Sellmeier oscillator model and Miller's rule for possible application in optical components and devices.

Author contributions

MME contributed to conceptualization, methodology, software, validation, formal analysis, investigation, resources, data curation, writing—original draft, writing—review and editing, visualization, and supervision. MTA performed conceptualization and revised the manuscript. KAA contributed to UV/Vis and ATR-FTIR measurements. MAA contributed to TGA/DTA measurements. TF performed formal analysis, investigation, and writing—review and editing.

Funding

Data availability

The data that support the findings of this study are available on request from the corresponding author.

Declarations

Conflict of interest The authors declare that they have no known competing financial interests or personal relationships that could have appeared to influence the work reported in this paper. The authors declare that they have no conflict of interest.

References

1. A. Dawelbeit, M. Yu, Materials **14**, 2938–2960 (2021). https://doi.org/10.3390/ma14112938

2. K.S. Ngai, S. Ramesh, K. Ramesh, J.C. Juan, Ionics **22**, 1259–1279 (2016). https://doi.org/10.1007/S11581-016-1756-4

3. W. Li, Y. Pang, J. Liu, G. Liu, Y. Wang, Y. Xia, RSC Adv. **7**, 23494–23501 (2017). https://doi.org/10.1039/C7RA02603J

4. C. Sequeira, D. Santos, *Polymer Electrolytes: Fundamentals and Applications*, 1st edn. (Woodhead Publishing Limited, Sawston, 2010)

5. F. Jäkle, Chem. Rev. **110**, 3985–4022 (2010). https://doi.org/10.1021/CR100026F

6. L.H. Slooff, A. Van Blaaderen, A. Polman, G.A. Hebbink, S.I. Klink, F.C.J.M. Van Veggel, D.N. Reinhoudt, J.W. Hofstraat, J. Appl. Phys. **91**, 3955 (2002). https://doi.org/10.1063/1.1454190

7. A.Y. Yassin, A.M. Abdelghany, M.M. Shaban, Y.M. Abdallah, Colloids Surf. A **635**, 128115 (2022). https://doi.org/10.1016/J.COLSURFA.2021.128115

8. L. Zhang, J.-H. Yang, X.-Y. Wang, X. He, B. Zhao, Z.-H. Tang, G.-Z. Yang, H.-X. Qiu, Chin. Phys. Lett. **28**, 016501 (2011). https://doi.org/10.1088/0256-307X/28/1/016501

9. N.S. Schauser, A. Nikolaev, P.M. Richardson, S. Xie, K. Johnson, E.M. Susca, H. Wang, R. Seshadri, R.J. Clément, J.R. de Alaniz, R.A. Segalman, ACS Macro Lett. **10**, 104–109 (2021). https://doi.org/10.1021/acsmacrolett.0c00788

10. D.K. Pradhan, R.N.P. Choudhary, B.K. Samantaray, N.K. Karan, R.S. Katiyar, Int. J. Electrochem. Sci. **2**, 861–871 (2007)

11. J. Imbrogno, K. Maruyama, F. Rivers, J.R. Baltzegar, Z. Zhang, P.W. Meyer, V. Ganesan, S. Aoshima, N.A. Lynd, ACS Macro Lett. **10**, 1002–1007 (2021). https://doi.org/10.1021/ACSMACROLETT.1C00305

12. B.K. Money, K. Hariharan, J. Swenson, J. Phys. Chem. B **116**, 7762–7770 (2012). https://doi.org/10.1021/JP3036499

13. K. Pielichowski, J. Njuguna, *Thermal Degradation of Polymeric Materials* (Rapra Technology Limited, London, 2005)

14. S. Gangadharan, A. Sujith, V. Anbazhagan, Chem. Methodol. **5**, 555–564 (2021). https://doi.org/10.22034/CHEMM.2021.138939

15. V.R. Hokmabad, S. Davaran, M. Aghazadeh, E. Alizadeh, R. Salehi, A. Ramazani, Tissue Eng. Regen. Med. **15**, 735–750 (2018). https://doi.org/10.1007/S13770-018-0140-Z/FIGURES/10

16. U. Shinde, S. Patil, R. Thorave, D. Malkhede, Chem. Methodol. **5**, 471–484 (2021). https://doi.org/10.22034/CHEMM.2021.138070

17. M.R.R. Prasad, K. Krishnan, K.N. Ninan, V.N. Krishnamurthy, Thermochim. Acta. **297**, 207–210 (1997). https://doi.org/10.1016/S0040-6031(96)03070-5

18. S. Ramesh, S.C. Lu, E. Morris, J. Taiwan Inst. Chem. Eng. **43**, 806–812 (2012). https://doi.org/10.1016/J.JTICE.2012.04.004

19. R. Biczak, B. Pawłowska, M. Płatkowski, M. Stręk, A. Telesiński, Bull. Environ. Contam. Toxicol. **98**, 567–573 (2017). https://doi.org/10.1007/S00128-017-2033-6/TABLES/2

20. M. Ahmed, T. Fahmy, J. Korean Phys. Soc. **59**, 98–104 (2011). https://doi.org/10.3938/jkps.59.98

21. T. Fahmy, Polym. Plast. Technol. Eng. **46**, 7–18 (2007). https://doi.org/10.1080/03602550600915136

22. M. Ahmed, T. Fahmy, Polym. Plast. Technol. Eng. **44**, 1559–1572 (2005). https://doi.org/10.1080/03602550500209507

23. T. Fahmy, A. Sarhan, I.A. Elsayed, H.G. Abdelwahed, Int. J. Eng. Res. Technol. **11**, 1405–1415 (2018)

24. A.M. Abdelghany, M.A. Morsi, A. Abdelrazek, SILICON **10**, 1697–1704 (2018). https://doi.org/10.1007/s12633-017-9655-5

25. A.Y. Yassin, A.R. Mohamed, E.M. Abdelrazek, M.A. Morsi, A.M. Abdelghany, J. Mater. Res. Technol. **8**, 1111–1120 (2019). https://doi.org/10.1016/J.JMRT.2018.08.005

26. M.M. Elmahdy, T. Fahmy, K.A. Aldhafeeri, E.O. Ibnouf, Y. Riadi, Mater. Chem. Phys. **264**, 124369 (2021). https://doi.org/10.1016/J.MATCHEMPHYS.2021.124369

27. G. Socrates, *Infrared and Raman Characteristic Group Frequencies: Tables and Charts* (Wiley, Hoboken, 2004)

28. E. Ruckenstein, Y. Yuan, Polymer **38**, 3855–3860 (1997). https://doi.org/10.1016/S0032-3861(96)00939-1

29. E. Vargün, A. Usanmaz, J. Polym. Sci. Part A **43**, 3957–3965 (2005). https://doi.org/10.1002/POLA.20867

30. L. Costa, M. Avataneo, P. Bracco, V. Brunella, Polym. Degrad. Stab. **77**, 503–510 (2002). https://doi.org/10.1016/S0141-3910(02)00108-8

31. M. Füllbrandt, P.J. Purohit, A. Schönhals, Macromolecules **46**, 4626–4632 (2013). https://doi.org/10.1021/MA400461P

32. M.R. Jung, F.D. Horgen, S.V. Orski, V. Rodriguez, K.L. Beers, G.H. Balazs, T.T. Jones, T.M. Work, K.C. Brignac, S.J. Royer, K.D. Hyrenbach, B.A. Jensen, J.M. Lynch, Mar. Pollut. Bull. **127**, 704–716 (2018). https://doi.org/10.1016/J.MARPOLBUL.2017.12.061

33. G. Sivalingam, R. Karthik, G. Madras, Ind. Eng. Chem. Res. **42**, 3647–3653 (2003). https://doi.org/10.1021/IE030009K

34. Z. Xu, S.S. Kolapkar, S. Zinchik, E. Bar-Ziv, A.G. McDonald, Polym. Degrad. Stab. **176**, 109148 (2020). https://doi.org/10.1016/J.POLYMDEGRADSTAB.2020.109148

35. M.S. Abbas-Abadi, J. Therm. Anal. Calorim. **143**, 2867–2882 (2021). https://doi.org/10.1007/S10973-020-09344-0/FIGURES/13

36. A. Marongiu, T. Faravelli, G. Bozzano, M. Dente, E. Ranzi, J. Anal. Appl. Pyrol. **70**, 519–553 (2003). https://doi.org/10.1016/S0165-2370(03)00024-X

37. S.M. Kuznetsov, E.A. Sagitova, K.A. Prokhorov, G.Y. Nikolaeva, D.I. Mendeleev, P. Donfack, A. Materny, Spectrochim. Acta Part A **252**, 119494 (2021). https://doi.org/10.1016/J.SAA.2021.119494

38. D. Torres, Y. Jiang, D.A. Sanchez-Monsalve, G.A. Leeke, J. Anal. Appl. Pyrolysis. **149**, 104831 (2020). https://doi.org/10.1016/J.JAAP.2020.104831

39. J. Zhou, G. Liu, S. Wang, H. Zhang, F. Xu, J. Energy Inst. **93**, 2362–2370 (2020). https://doi.org/10.1016/J.JOEI.2020.07.009

40. M.N. Radhakrishnan Nair, G.V. Thomas, M.R. Gopinathan Nair, Polym. Degrad. Stab. **92**, 189–196 (2007). https://doi.org/10.1016/J.POLYMDEGRADSTAB.2006.11.014

41. M. Akçay, J. Colloid Interface Sci. **296**, 16–21 (2006). https://doi.org/10.1016/J.JCIS.2005.08.031

42. J. De La Zerda, R. Neumann, Y. Sasson, J. Chem. Soc. Perkin Trans. **2**, 823–826 (1986). https://doi.org/10.1039/P29860000823

43. L.T. Vlaev, I.G. Markovska, L.A. Lyubchev, Thermochim. Acta. **406**, 1–7 (2003). https://doi.org/10.1016/S0040-6031(03)00222-3

44. H.L. Friedman, J. Polym. Sci. Part C **6**, 183–195 (1964). https://doi.org/10.1002/POLC.5070060121

45. A.W. Coats, J.P. Redfern, Nature **201**, 68–69 (1964). https://doi.org/10.1038/201068a0

46. S. Altarawneh, M. Al-Harahsheh, C. Dodds, A. Buttress, S. Kingman, Thermochim. Acta. **707**, 179105 (2022). https://doi.org/10.1016/J.TCA.2021.179105

47. R.K. Agrawal, J. Therm. Anal. Calorim. **31**, 73–86 (1986). https://doi.org/10.1007/BF01913888

48. L. Liu, Q.X. Guo, Chem. Rev. **101**, 673–695 (2001). https://doi.org/10.1021/CR990416Z

49. M.D. Migahed, M.T. Ahmed, A.E. Kotp, J. Phys. D **33**, 2108–2116 (2000). https://doi.org/10.1088/0022-3727/33/17/304

50. P.H. Daniels, J. Vinyl Addit. Technol. **15**, 219–223 (2009). https://doi.org/10.1002/vnl.20211

51. P.W. Skelly, L. Li, R. Braslau, Polym. Rev. **62**, 485–528 (2021). https://doi.org/10.1080/15583724.2021.1986066

52. T. Rezende, C. Abreu, A. Fonseca, C. Higa, L. Li, A. Serra, R. Braslau, J. Coelho **196**, 122473 (2020). https://doi.org/10.1016/j.polymer.2020.122473

53. L. Li, A. Tek, R. Wojtecki, B. Rebecca, J. Polym. Sci. A **57**, 1821–1835 (2019). https://doi.org/10.1002/pola.29455

54. Y. Ma, S. Liao, Q. Li, Q. Guan, P. Jia, React. Funct. Ploym. **147**, 104458 (2020). https://doi.org/10.1016/j.reactfunctpolym.2019.104458

55. J. Czogała, E. Pankalla, R. Turczyn, Materials (Basel) **14**, 1–28 (2021). https://doi.org/10.3390/MA14040844

56. R. Navarro, M. Pérez Perrino, C. García, C. Elvira, A. Gallardo, H. Reinecke, Macromolecules **49**, 2224–2227 (2016). https://doi.org/10.1021/ACS.MACROMOL.6B00214

57. R. Navarro, T. Gacal, M. Ocakoglu, C. García, C. Elvira, A. Gallardo, H. Reinecke, Macromol. Rapid Commun. **38**, 1600734 (2017). https://doi.org/10.1002/MARC.201600734

58. J. Tauc, A. Menth, J. Non. Cryst. Solids. **8–10**, 569–585 (1972). https://doi.org/10.1016/0022-3093(72)90194-9

59. F. Urbach, Phys. Rev. **92**, 1324 (1953). https://doi.org/10.1103/PhysRev.92.1324

60. N.F. Mott, E.A. Davis, *Electronic Processes in Non-crystalline Materials*, 2nd edn. (Oxford University Press Inc., Oxford, 1979)

61. J. Tauc, R. Grigorovici, A. Vancu, Phys. Status Solidi. **15**, 627–637 (1966). https://doi.org/10.1002/PSSB.19660150224

62. H. Najafi-Ashtiani, A. Bahari, Synth. Met. **217**, 19–28 (2016). https://doi.org/10.1016/J.SYNTHMET.2016.03.008

63. H. Najafi-Ashtiani, A. Bahari, Opt. Mater. (Amst). **58**, 210–218 (2016). https://doi.org/10.1016/J.OPTMAT.2016.05.035

64. C.U. Devi, A.K. Sharma, V.V.R.N. Rao, Mater. Lett. **56**, 167–174 (2002). https://doi.org/10.1016/S0167-577X(02)00434-2

65. J.I. Pankove, *Optical Processes in Semiconductors* (Prentice-Hall, Inc., Englewood Cliffs, 1971)

66. F. Wooten, Am. J. Phys. **41**, 939 (1973). https://doi.org/10.1119/1.1987434

67. S.H. Wemple, Phys. Rev. B **7**, 3767 (1973). https://doi.org/10.1103/PhysRevB.7.3767

68. S.H. Wemple, M. Didomenico, Phys. Rev. Lett. **23**, 1156 (1969). https://doi.org/10.1103/PhysRevLett.23.1156

69. S.H. Wemple, M. DiDomenico, Phys. Rev. B **3**, 1338–1351 (1971). https://doi.org/10.1103/PhysRevB.3.1338

70. P. Atkins, J. de Paula, *Physical Chemistry*, 10th edn. (Oxford University Press, Oxford, 2014)

71. E.I. Izgorodina, M. Forsyth, D.R. MacFarlane, Phys. Chem. Chem. Phys. **11**, 2452–2458 (2009). https://doi.org/10.1039/B815835E

72. P.A. Lee, G. Said, R. Davis, T.H. Lim, J. Phys. Chem. Solids. **30**, 2719–2729 (1969). https://doi.org/10.1016/0022-3697(69)90045-6

73. D. Cotter, R.J. Manning, K.J. Blow, A.D. Ellis, A.E. Kelly, D. Nesset, I.D. Phillips, A.J. Poustie, D.C. Rogers, Science (80-) **286**, 1523–1528 (1999). https://doi.org/10.1126/science.286.5444.1523

74. R.W. Boyd, *Nonlinear Optics* (Academic Press, New York, 2020)

75. H. Tichá, L. Tichý, J. Optoelectron. Adv. Mater. **4**, 381–386 (2002)

76. N. Sharma, S. Sharda, V. Sharma, P. Sharma, Mater. Chem. Phys. **136**, 967–972 (2012). https://doi.org/10.1016/J.MATCHEMPHYS.2012.08.034

77. Z. Jin, D. Gehrig, C. Dyer-Smith, E.J. Heilweil, F. Laquai, M. Bonn, D. Turchinovich, J. Phys. Chem. Lett. **5**, 3662–3668 (2014). https://doi.org/10.1021/JZ501890N

78. G. Jian, Y. Jiao, L. Feng, Q. Meng, N. Yang, S. Zhu, M. Lü, C.P. Wong, NPG Asia Mater. **14**, 1–11 (2022). https://doi.org/10.1038/s41427-022-00356-w

79. F. Kremer, A. Schönhals, *Broadband Dielectric Spectroscopy* (Springer, Berlin, 2002)